Research Article | Vol. 33, No. 12 / 16 Jun 2025 / Optics Express 25580
Optics EXPRESS

Tunable unidirectional large-area surface magnetoplasmons in a stratified waveguide

QIAN SHEN,[1] YUN YOU,[2] ZHENGMING TANG,[1] JINWEI GAO,[1,4] AND JIE XU[3,5]

[1]School of Electronic Information Engineering, China West Normal University, Nanchong, 637002, China
[2]School of Science, East China Jiaotong University, Nanchang, 330031, China
[3]School of Medical Information and Engineering, Southwest Medical University, Luzhou, 646000, China
[4]jwgao@cwnu.edu.cn
[5]xujie011451@163.com

Abstract: Large-area unidirectional modes have attracted increasing attention due to their potential applications in wave manipulation; however, most implementations are constrained by poor adjustment capability or narrow operating bandwidth, since minor structural parameter changes may significantly affect the one-way propagation range. In this work, we propose and investigate a robust and broadband unidirectional large-area surface magnetoplasmon (LSMP) mode in a stratified waveguide consisting of magnetized yttrium iron-garnet, air, and μ-negative materials. Through theoretical analysis and numerical simulations, we demonstrate that the electric field with uniform amplitude and a nearly flat phase profile can be achieved in the tunable one-way range by adjusting the filling ratio of μ-negative materials. Relying on this unique electric field distribution, we demonstrate beam focusing, Bessel beam generation, and an adjustable beam splitter using LSMP modes. These results are expected to be applied in the field of all-optical communication and imaging, such as efficient holographic imaging.

1. Introduction

Metamaterials, as an innovative class of artificial composites, exhibit extraordinary physical properties that have led to their rapid expansion both in research endeavours and in practical applications. These advanced materials leverage meticulously designed microstructures to precisely manipulate waves, including acoustic and electromagnetic (EM) waves, showcasing potential in diverse fields including information communication, stealth technology, and energy harvesting [1–3]. Among them, μ-near-zero (MNZ) and μ-negative (MNG) metamaterials have attracted considerable attention due to their distinct EM response characteristics. MNZ materials enable significantly reduce EM wave scattering [4,5], while MNG materials offer extraordinary manipulation of EM waves [6,7], thereby establishing a solid theoretical framework for novel functional devices. More recently, the integration of metamaterials with sonic crystals has facilitated the achievement of large-area unidirectional acoustic wave transmission [8–10], presenting a novel paradigm for the design of high-capacity EM transmission systems. On the other hand, in EM transmission fields, unidirectional modes propagate solely in a single direction, thus enhancing the efficiency and reliability of such systems through the elimination of the phenomenon of backscattering [11–16]. However, these modes are typically limited to very narrow channels, making large-area unidirectional waves pivotal for practical applications.

Research on large-area unidirectional EM modes is primarily categorized into two approaches: those that utilize large-area photonic crystal (LPhC) modes in photonic crystals [17–27], and those that employ surface magnetoplasmons (SMPs) in magneto-optical waveguide [28,29]. Recent studies on LPhC modes have been inspired by profound quantum mechanical phenomena such as quantum Hall effects [17,18], quantum-spin-Hall effects [19,20], and quantum-valley-Hall effects [25], etc. For instance, Ref. [17] highlighted the crucial role of Dirac cones in the middle domain

#563713 https://doi.org/10.1364/OE.563713
Journal © 2025 Received 28 Mar 2025; revised 29 May 2025; accepted 29 May 2025; published 6 Jun 2025

Optics EXPRESS

for the strong coupling and hybridization of two topological interface states, while Ref. [19] employed PhCs featuring double Dirac cones to achieve LPhC modes. However, the scaling laws governing the operational bandwidth as a function of the width of the middle domain in these systems are not yet known. On the other hand, SMPs offer a promising approach for constructing stable and efficient large-area modes. By minimizing the transverse attenuation coefficients of the fields within the middle domain, large-area SMPs (LSMPs) have been successfully demonstrated [28,29]. However, enhancing transmission width often incurs a trade-off with operating bandwidth, as exemplified by an LSMP mode with a limited operational bandwidth of $0.03\omega_m$ (where ω_m represents the plasmonic resonance frequency) [28]. Despite their simpler structural configuration and enhanced stability, further research is crucial to address the narrow operational bandwidth of LSMPs and explore their potential applications in a broader context.

In this paper, a tunable LSMP approach utilizing stratified waveguides is proposed. This configuration under consideration consists of magnetized yttrium-iron-garnet (YIG) and periodic alternating layers of air and MNG materials. Leveraging effective medium theory [30,31], we conduct a comprehensive analysis to understand how the system parameters relate to the modal size of LSMP and the unidirectional bandwidth of the system. Our findings reveal that the proposed system can achieve a balance between operating bandwidth and critical modal size, leading to a significant enhancement in bandwidth compared to previous LSMP designs. Furthermore, the proposed LSMP maintains a uniform electric field distribution (both in amplitude and phase) across the entire unidirectional propagating band and exhibits strong robustness against various defects. Based on these unique characteristics, we further explore potential applications of the proposed LSMP in wavefront manipulation, such as beam focusing and Bessel-beam generation. To underscore the versatility of this design, we propose a beam splitter with adjustable splitting ratios. Our findings fully demonstrate the broad potential applications of LSMPs in multiple fields, including communication, imaging, and sensing technologies.

2. Physical structure and modal properties

The fundamental model of the proposed structure is depicted in Fig. 1(a). The central region of the system, with a thickness d, consists of periodic alternating layers of air and μ-negative (MNG) materials. The period of the air-MNG (AM) array is 1 mm, significantly smaller than the wavelength. In one period, the thickness of air and the MNG medium is denoted as d_A and d_M, respectively. According to effective medium theory, the AM arrays can be described by an effective relative permeability tensor expressed in the following form:

$$\mu_{\mathbf{AM}} = \begin{bmatrix} \mu_{ex} & 0 & 0 \\ 0 & \mu_{ey} & 0 \\ 0 & 0 & \mu_{ey} \end{bmatrix} \tag{1a}$$

with

$$\mu_{ex} = p(\mu_M - \mu_A) + \mu_A, \tag{1b}$$

$$\mu_{ey} = \frac{\mu_A \mu_M}{p(\mu_A - \mu_M) + \mu_M}, \tag{1c}$$

where μ_M and μ_A are the relative permeability of the MNG media and air, and $p = d_M/(d_A + d_M)$ is the filling ratio of the MNG media. In this waveguide structure, the two YIG layers, each with a permittivity ε_{YIG} of 15, are subjected to a pair of external static magnetic fields of equal magnitude but opposite directions. These magnetic fields induce gyromagnetic anisotropy in the

Optics EXPRESS

YIG, resulting in a permeability tensor expressed as follows:

$$\mu_{\mathbf{YIG}} = \begin{bmatrix} \mu_1 & \mp\mu_2 & 0 \\ \pm\mu_2 & \mu_1 & 0 \\ 0 & 0 & 1 \end{bmatrix} \tag{2}$$

where $\mu_1 = 1 + \omega_m(\omega_0 - i\nu\omega)/((\omega_0 - i\nu\omega)^2 - \omega^2)$, $\mu_2 = \omega_m\omega/((\omega_0 - i\nu\omega)^2 - \omega^2)$, with ω_m being the characteristic angular frequency and $\omega_0 = 2\pi\gamma H_0$ being the precession circular frequency, and γ and ν denoting the gyromagnetic ratio and damping coefficient. To distinguish guiding mode (real propagation constant) from evanescent mode (with complex propagation constant), we initially assume $\nu = 0$ in dispersion calculations. Material loss, i.e., $\nu = 0.001$, is subsequently incorporated in wave-transmission analyses. In magnetized YIG, the bulk modes exhibit a dispersion relation specific to transverse-electric (TE) polarization, given by $k = \sqrt{\varepsilon_{YIG}\mu_v}k_0$, where k is the propagation constant, k_0 is the vacuum wavenumber, and $\mu_v = \mu_1 - \mu_2^2/\mu_1$ represents the Voigt permeability. Consequently, the magnetized YIG features a single bandgap defined by μ<0. The bulk-mode bandgap spans from ω_a to ω_b, where $\omega_a = \sqrt{\omega_0(\omega_0 + \omega_m)}$ and $\omega_b = \omega_0 + \omega_m$. In this paper, we consider $\omega_m = 2\pi \times 5 \times 10^9$ rad/s, which corresponds to $\lambda_m = 60$ mm.

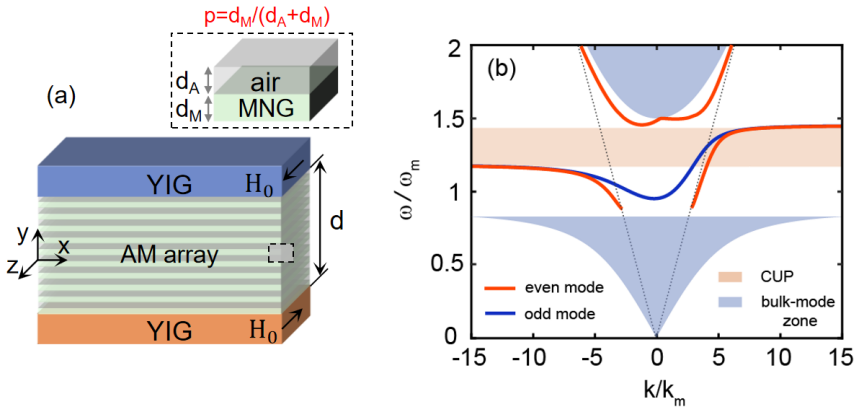

Fig. 1. (a) Schematic of the stratified waveguide, the dashed box is a unit of the AM array. (b) Dispersion relations of guiding modes. Red and blue lines are the dispersion curves for even and odd modes. Dashed lines are the effective light line in the AM layer, where $\mu_{ex} = 0.05$, $\mu_{ey} = 10$. The upper and lower shaded areas represent the zones of bulk modes in the YIG, and the middle shaded area indicate the CUP region. The other parameters are $\omega_0 = 0.5\omega_m$, $d = 2\lambda_m$.

The SMP modes that arise within the bulk-mode bandgap are characterized by TE polarization. They can be categorized into even and odd modes, distinguished by their symmetric and antisymmetric electric field distributions, respectively. Their dispersion relation for SMP modes can be derived as

$$\frac{\alpha_{YIG} + \mu_2 k}{\alpha_{AM}\mu_v}\mu_{ex} + \tanh\frac{\alpha_{AM}d}{2} = 0, \tag{3a}$$

$$\frac{\alpha_{YIG} + \mu_2 k}{\alpha_{AM}\mu_v}\mu_{ex} + \coth\frac{\alpha_{AM}d}{2} = 0, \tag{3b}$$

Optics EXPRESS

for even and odd mode, where $\alpha_{AM} = \sqrt{\mu_{ex}(k^2/\mu_{ey} - k_0^2)}$ and $\alpha_{YIG} = \sqrt{k^2 - \varepsilon_{YIG}\mu_v k_0^2}$ are respectively the attenuation coefficient of the field in the AM region and YIG. It is well-established that the SMP dispersions are defined by their asymptotic frequencies, at which $k \to \pm\infty$. From Eqs. (3), we observe that only one asymptotic frequency emerges for $k>0$ (ω_{sp^+}) and $k<0$ (ω_{sp^-}). Detailed derivations of these results are provided in Supplement 1. This indicates that unidirectional SMPs are only allowed to propagate in the frequency range $\left[\omega_{sp}^-, \omega_{sp}^+\right]$. We emphasize that material loss has a negligible impact on dispersion relation except for a very small interval near the asymptotic frequencies. Importantly, this negligible effect does not alter the unidirectional transmission range of interest for our system [32].

To clearly illustrate the guiding modes in our structure, we numerically calculated the SMP dispersion relations with Eqs. (3). As an illustrative example, we selected the parameters $\mu_{ex} = 0.05$, $\mu_{ey} = 10$, and $\omega_0 = 0.5\omega_m$, $d = 2\lambda_m$ (where λ_m is the vacuum wavelength for ω_m). Figure 1(b) displays the dispersion relations for both even and odd modes. For even mode, the lower two branches are SMP modes, which are characterized by different asymptotic frequencies. The uppermost branch is categorized as a regular mode, which is guided by total internal reflection between the YIG-AM interfaces. The regular mode has a lower cutoff frequency, denoted as ω_{cf}. For odd mode, its dispersion features a single dispersion band encompassing two asymptotic frequencies, which coincide with those identified for the even SMP mode. As expected, SMPs only propagate in the forward direction within the specific frequency range $\left[\omega_{sp}^-, \omega_{sp}^+\right]$, resulting in the phenomenon referred to complete unidirectional propagation (CUP) within the waveguide. However, as seen in Fig. 1(b), the value of ω_{cf} has a significant impact on CUP bandwidth ($\Delta\omega_{CUP}$). It can be expressed as $\Delta\omega_{CUP} = \omega_{sp}^+ - \omega_{sp}^-$ for $\omega_{cf} \geq \omega_{sp}^+$, otherwise $\Delta\omega_{CUP} = \omega_{cf} - \omega_{sp}^-$ for $\omega_{cf} < \omega_{sp}^+$. Notably, for the present system, only even mode is of our interest, since the E-field amplitude of the odd mode diminishes at the waveguide axis ($y = 0$). So our subsequent analysis will focus on the even mode.

We first analyzed the situation for $\omega_{cf} \geq \omega_{sp}^+$, where $\Delta\omega_{CUP} = \omega_{sp}^+ - \omega_{sp}^-$. As discussed above, ω_{sp}^+ and ω_{sp}^- are closely dependent on ω_0 and the product of μ_{ex} and μ_{ey}. Therefore, we examined the dependence of the CUP range on ω_0 and δ ($\delta = \mu_{ex}\mu_{ey}$) using Eqs. (4) and (5), and the results are presented in Fig. 2. In Fig. 2(a), the parameters are: $\delta = 0.5$, and $d = 2\lambda_m$. The upper and lower boundaries in Fig. 2 are delineated by the forward and backward asymptotic frequencies, respectively. As seen in Fig. 2(a), $\Delta\omega_{CUP}$ is decreasing with the increase of ω_0, a result that may appear counterintuitive. This phenomenon can be attributed to the persistence of remanence in YIG even after the removal of an (external) magnetic field. Therefore, to maintain the tunability of (external) magnetic field while optimize the CUP bandwidth, in what follows, we take $\omega_0 = 0.1\omega_m$. In this scenario, $\Delta\omega_{CUP} = 0.365\omega_m$. Figure 2(b) shows the CUP range versus δ for the case of $\omega_0 = 0.1\omega_m$. Both ω_{sp}^+ and ω_{sp}^- exhibit a decreasing trend as δ increases, with the decrease in ω_{sp}^- being more significant than that in ω_{sp}^+. As a result, ω_{CUP} ultimately experiences an increase with the increase of δ. Our numerical calculation indicate that for $\delta = 1$, $\Delta\omega_{CUP}$ is increased to $0.427\omega_m$, which is ten times than that reported in Ref. [28]. Though a larger δ would lead to a larger $\Delta\omega_{CUP}$, it will challenge the current manufacturing technology of metamaterials. Therefore, from the point of view of actual manufacturing, we will restrict our structure in the following text with the optimized parameters, i.e., $\omega_0 = 0.1\omega_m$ and $\delta = 1$. For simplify, the MNG material is taken as $\mu_M = -1$, thus $\mu_{ex} = -2p + 1$ and $\mu_{ey} = 1/(-2p + 1)$, with p being the filling ratio of MNG material. In this scenario, $\Delta\omega_{CUP}$ is unaffected by p, since $\mu_{ex}\mu_{ey}$ is always equal to 1.

Let's examine the situation for $\omega_{cf} < \omega_{sp}^+$. In this scenario, the regular modes are typically demonstrated bidirectional propagation, which consequently constrains the upper limit of the CUP band. This is an undesirable situation. To mitigate this occurrence, it is necessary to suppress the regular modes above ω_{sp}^+. The dispersion relation for regular modes can be obtained

Optics EXPRESS

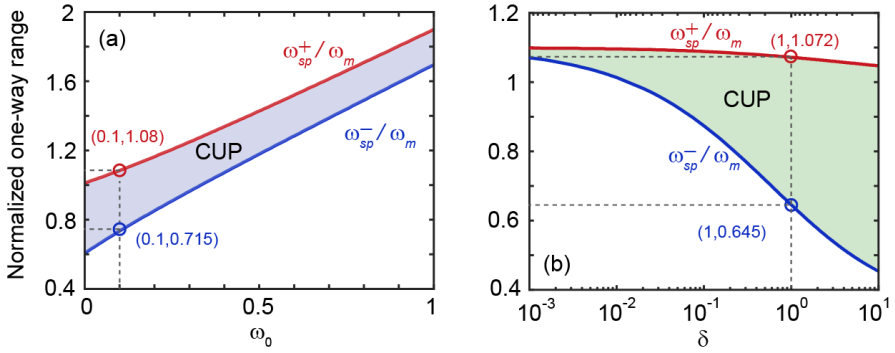

Fig. 2. (a) Complete one-way range versus ω_0. The parameters are $\mu_{ex} = 0.05$, $\mu_{ey} = 10$. (b) Complete one-way range versus δ ($\delta = \mu_{ex}\mu_{ey}$) for the case $\omega_0 = 0.1\omega_m$.

from Eq. (3) by substituting $\alpha_{AM} = -i\beta$, where $\beta = \sqrt{\mu_{ex}(k_0^2 - k^2/\mu_{ey})}$. Each regular mode is associated with a transverse resonance of a specific order in the AM layers, and thus, the cutoff frequency ω_{cf} is expected to be determined by the parameter d. Though the regular modes in the present guiding system are nonreciprocal, ω_{cf} should very close to $k = 0$. Therefore, the conditions for their existence can be deduced by examining the dispersion equation at $k = 0$. At $k = 0$, the dispersion equation simplifies to:

$$1 + \sqrt{\frac{-\mu_v}{\varepsilon_{YIG}\mu_{ex}}}\, tan\left(\frac{\beta d}{2}\right) = 0. \tag{4}$$

Within the YIG bandgap, μ_v<0; thus a solution to Eq. (4) exists only when $\beta d/2 \in [\pi/2 + n\pi, (n+1)\pi]$, where $n = 0, 1, 2, \ldots$. Therefore, the suppression condition for the regular modes should be $\beta d/2 < \pi/2$, where $\beta \approx \sqrt{\mu_{ex}}\omega_{sp}^{+}/c$. From this condition, the critical thickness d_c is obtained as

$$d_c = \frac{\pi c}{\omega_{sp}^{+}\sqrt{-2p+1}}. \tag{5}$$

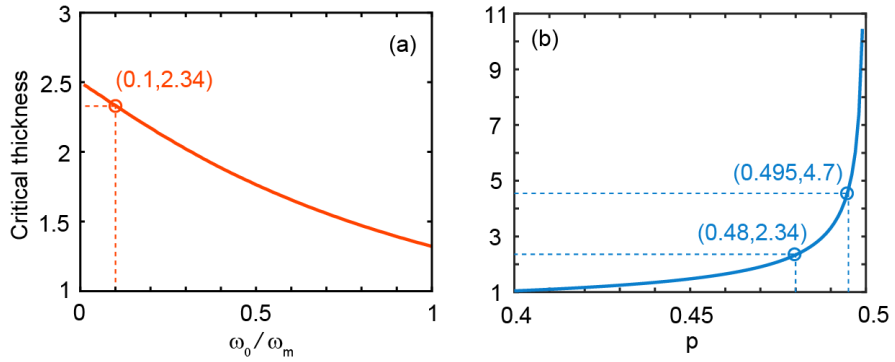

Fig. 3. (a) Critical thickness of LSMP as a function of ω_0 for $p = 0.48$ (where $\mu_{ex} = 0.04$ and $\mu_{ey} = 25$). (b) Critical thickness of LSMP as a function of p for $\omega_0 = 0.1\omega_m$.

Evidently, d_c is a function of ω_{sp}^{+}, which closely depends on the external magnetic field (ω_0) and the filling ratio of MNG material (p). Figure 3(a) illustrates the dependence of d_c on ω_0. In Fig. 3(a), we take $p = 0.48$, where $\mu_{ex} = 0.04$ and $\mu_{ey} = 25$. It is shown that d_c exhibits a

Optics EXPRESS

decreasing trend as ω_0 increases, thereby underscoring the importance of selecting a smaller ω_0. Figure 3(b) displays the dependence of d_c on p, showing that d_c increases with increasing p. Specifically, as p grows from 0.48 to 0.495, d_c increases from $2.34\lambda_m$ (140.4 mm) to $4.7\lambda_m$ (282 mm). This substantial thickness is notable, since the penetration depth of a regular SMP mode in YIG layer is only $0.16\lambda_m$ (9.8 mm). Notably, d_c becomes larger as p approaches 0.5. Given that $\Delta\omega_{CUP}$ remains unaffected by variations in p, it is possible to attain a substantial modal size of LSMP while simultaneously preserving CUP bandwidth. This characteristic represents a significant advantage over previous studies in the literature.

3. Robust transmission of the LSMPs

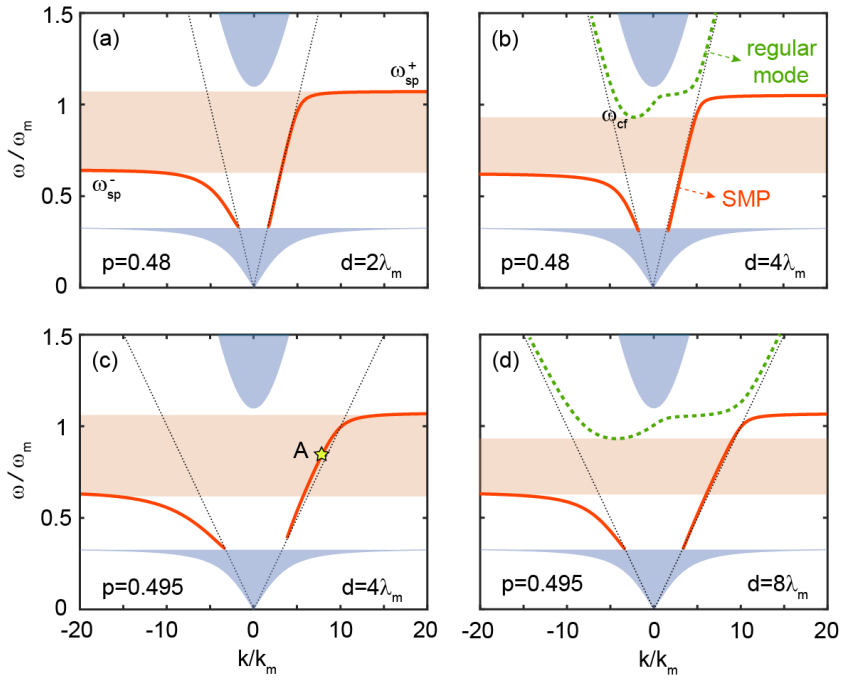

Fig. 4. Dispersion diagrams for the waveguides with different AM structures. (a) $p = 0.48$, $d = 2\lambda_m$; (b) $p = 0.48$, $d = 4\lambda_m$; (c) $p = 0.95$, $d = 4\lambda_m$; (d) $p = 0.95$, $d = 8\lambda_m$. The solid lines in each figure represent the dispersion curves of SMP in the waveguide, and the dashed lines in (b) and (d) represent regular modes. The other parameter is $\omega_0 = 0.1\omega_m$.

To validate our analysis above, we calculate the dispersion diagrams of SMPs for various p and d, with the representative results presented in Fig. 4. Figure 4(a) presents the dispersion diagram for $p = 0.48$, $d = 2\lambda_m$, and $\omega_0 = 0.1\omega_m$. In this case, $\Delta\omega_{CUP} = 0.427\omega_m$ and $d_c = 2.34\lambda_m$. As expected, only the SMP mode is observed in the bulk-mode bandgap. The CUP bandwidth is determined by ω_{sp}^+ and ω_{sp}^-, both of which experience a reduction; however, the overall bandwidth is augmented compared to that in Fig. 1(b). When $d>d_c$, a regular mode emerges, with its lower cutoff frequency ω_{cf} falling below ω_{sp}^+, as illustrated in Fig. 4(b) for the case where $d = 4\lambda_m$. Consequently, the CUP window experiences a compression from the upper boundary, which is dictated by ω_{cf}. Similar phenomena are observed in Figs. 4(c) and 4(d) for $p = 0.495$, $d = 4\lambda_m$ and $p = 0.495$, $d = 8\lambda_m$, respectively, where d_c is found to be $4.7\lambda_m$. As seen from Fig.4, the values of ω_{sp}^+ and ω_{sp}^- remain consistent across varying values of p, while an increase in p corresponds to a rise in d_c. All numerical results align closely with our analytical predictions. By

Optics EXPRESS

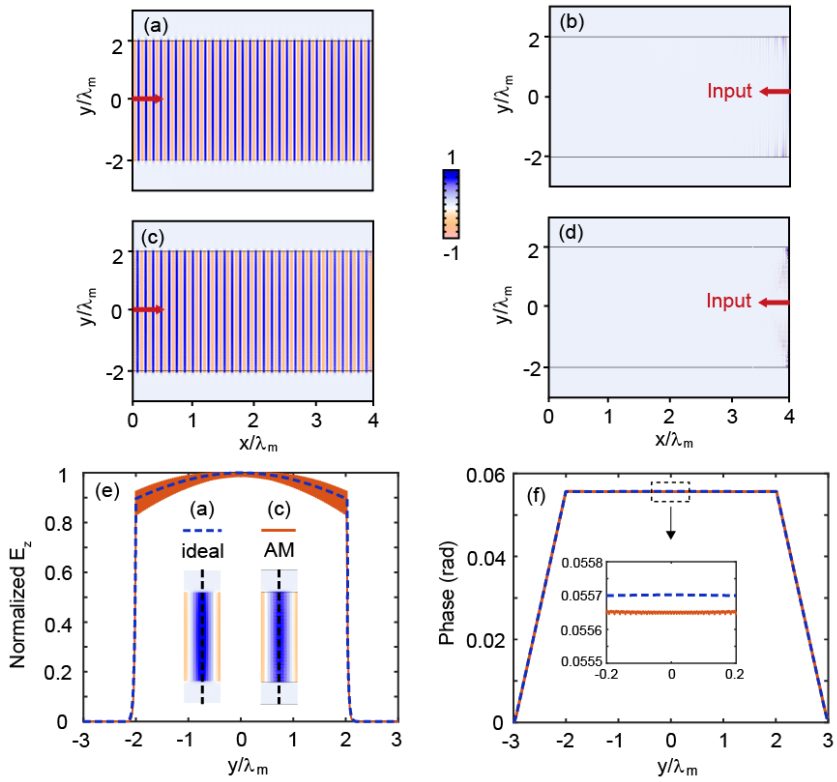

Fig. 5. Verification of unidirectional transmission and flat electric fields. (a-d) E-field distributions launched by a plane wave source at 4.3 GHz for different systems. (a) Ideal system and (c) AM system excited from the left port; (b) ideal system and (d) AM system excited from the right port. (e, f) The amplitude and phase distributions of the E-field along the y axis. The dashed and solid lines respectively represent distribution for the ideal and AM systems. The insets in (e) are close-up views in (a) and (c). The parameters are $d = 4\lambda_m$, $\omega_0 = 0.1\omega_m$, and $p = 0.495$.

combining all the above results, we will adopt the optimized parameters in Fig. 4(c), specifically $\omega_0 = 0.1\omega_m$, $p = 0.495$, for our subsequent analysis.

To further validate the guiding properties of the proposed structure, we performed wave simulations in it using the finite element method (FEM) for various scenarios. We began by simulating wave transmission in both a ideal homogeneous system and the designed AM system (with $\omega_0 = 0.1\omega_m$, $p = 0.495$). In these simulations, plane wave sources were employed to excite even modes, specifically at 4.3 GHz (marked by A in Fig. 4(c)). The sources were incident from the left boundaries of both systems. The resulting simulated E-field amplitudes are shown in Figs. 5(a) and 5(c) for the ideal and AM systems, respectively. The insets in Fig. 5(e) provide close-up views of these E-field distributions. It is evident that the E-field is uniformly distributed within the metamaterial regions, covering multiple wavelengths. This uniformity is further emphasized in Figs. 5(e) and 5(f), which depict the amplitude and phase distributions of the E-field along the dashed lines in the close-up sections. Therefore, the transverse modal size of the LSMP can be represented by d, and it is nearly $4\lambda_m$ for $d = 4\lambda_m$. Upon comparing the AM system to the idea case, it is shown that both the amplitude and phase distributions of the E-field in the AM system exhibit minimal oscillation and demonstrate a strong overall alignment. This observation supports the validity of the effective medium theory employed, suggesting that

Optics EXPRESS

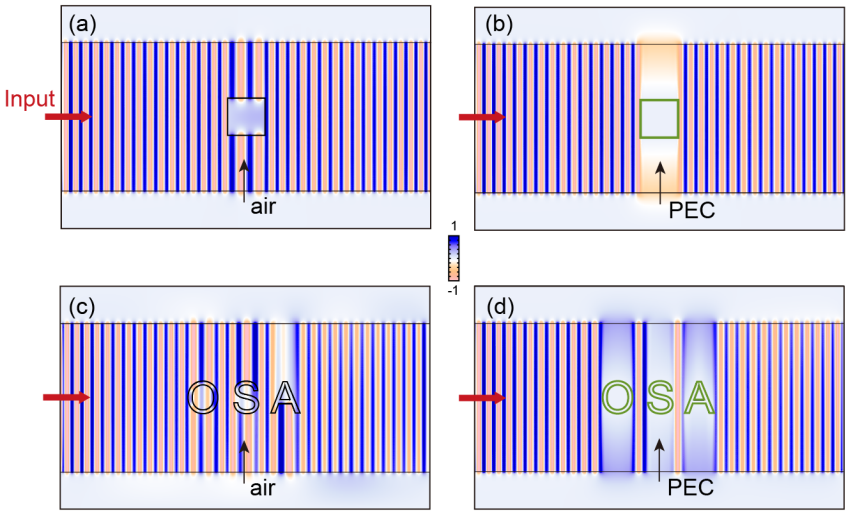

Fig. 6. Simulations for waveguides in the ideal system with different defects. (a) Air and (b) PEC defects with a square of side length λ_m; (c) air and (d) PEC defects with complex patterns "OSA". The parameters are the same as Fig. 5(a).

the two systems are indeed equivalent. Notably, the E-field amplitudes within the metamaterial regions display slight upward curvatures. This phenomenon can be attributed to the attenuation coefficient, denoted as $\alpha_{AM} = \sqrt{\mu_{ex}(k^2/\mu_{ey} - k_0^2)}$, which becomes imaginary under the specified parameters. Conversely, when the plane waves were incident from the right boundaries of both systems, transmission was prohibited, as shown in Figs. 5(b) and 5(d). These results provide compelling evidence of not only large-area but also unidirectional transport within the proposed structures. These ability is a significant advantage, facilitating the development of broad and isolated waveguiding channels that can be utilized in a range of applications, including isolators and other optical devices.

Next, we examine the resilience of LSMP transport in the presence of various defect types. All defects were positioned centrally within the waveguides. In Figs. 6(a) and 6(b), the defects are in the form of air and PEC columns, each with a square of side length λ_m. The simulation results of E-field amplitudes demonstrate a complete recovery of the LSMPs after traversing square defects containing air or PEC. These results closely resemble the defect-free scenario depicted in Fig. 5(a), implying that the square obstacles of air or PEC are invisible to the LSMPs. This distinctive characteristic is further exemplified in Figs. 6(c) and 6(d), which introduce more complex patterns, specifically the letters "OSA". The robustness of the one-way transport of LSMPs stems from the breaking of time-reversal symmetry. LSMPs demonstrate a remarkable resilience even in the presence of substantial and complex defects, highlighting their potential benefits in applications such as optical stealth technology.

4. Applications on tunable LSMPs

In this section, we illustrate the benefits of using LSMPs for beam control, particularly in terms of beam focusing, by employing the configuration shown in Fig. 7(a). In this setup, the outlet surface of the LSMP waveguide is engineered to function as a parabolic lens. To mitigate wave leakage along the YIG-air interfaces, thin PEC slabs are inserted between them. We performed this configuration using a full-wave FEM simulation, presenting the simulated intensity profiles for both ideal and AM systems in Figs. 7(c) and 7(d), respectively. In the

Optics EXPRESS

simulation, a plane wave incident from the left was utilized to excite the LSMPs at 4.3 GHz. The additional parameters include, $\omega_0 = 0.1\omega_m$, $p = 0.495$, and $d = 2\lambda_m$. It is noteworthy that the design concept is applicable across the entire CUP band, which, in this case, has a bandwidth of $0.43\omega_m$. Figures 7(c) and 7(d) depict the extraction and focusing of the waves into free space by the lens. Furthermore, the phase distributions of the extracted waves, as shown in Fig. 7(b), confirm adherence to a parabolic distribution. Additionally, our system demonstrates versatility through the simple alteration of the outlet surface of the LSMP waveguide. This feature enables the transition from focusing to alternative effects, such as the generation of a Bessel beam. To show the tunability of our system, we highlight that the focal length can be dynamically adjusted by varying: (1)the filling ratio of MNG material, (2)the external magnetic field strength (H0), and (3)the parabolic curvature of the outlet surface of the LSMP waveguide. This multi-path tunability enables precise control over the beam-splitting and focusing behavior, offering flexibility for diverse applications.

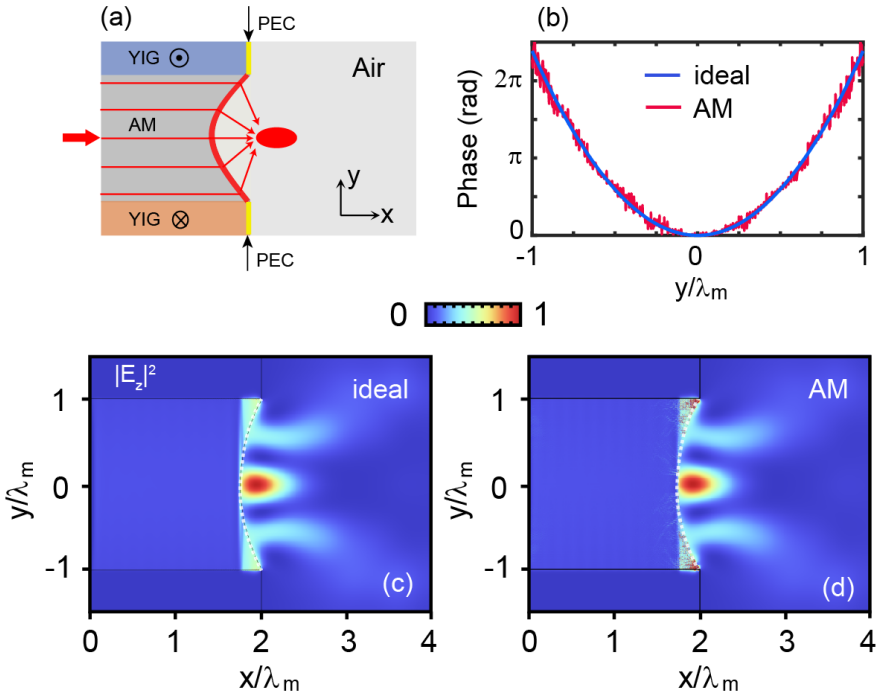

Fig. 7. (a) Schematic of beam focusing using LSMP waveguide. (b) The phase distribution of the extracted wave. (c, d)Simulated intensity profile $|E_z|^2$ of the ideal system and AM system.

Bessel beams, which are solutions to the Helmholtz equation, are characterized by their transverse amplitude distributions described by first-kind Bessel functions. These beams exhibit several remarkable properties, including non-diffraction, self-reconstruction, and possessing an ultra-narrow central spot radius ($\sim$ 1 wavelength). Such attributes make Bessel beams particularly advantageous for a wide range of applications in optics and photonics. Here, we numerically demonstrate the direct generation of Bessel beams from LSMPs by configuring the outlet surface of the LUSMP waveguide in the shape of a prism-type lens. This configuration is designed to impart a spatial phase profile characterized by the equation $\phi(y) = -\alpha\,|y|$, where $\alpha = k_0 sin\theta$ is the transverse wave number and θ is the angle at which radiation rays cross the optical axis. Due to limitations in computational resources, we have chosen the ideal model

Optics EXPRESS

for the generation of Bessel beams. Figures 8(a) and 8(b) respectively exhibit the simulated intensity profiles $|E_z|^2$ and $|H_x|^2$ at 4.3 GHz. The findings validate that the generated wave demonstrates distinct characteristics typical of a Bessel beam, particularly its non-diffracting properties. The observed maximum propagation distance of the Bessel beam is X_{max} = 102.6 mm. This value is in close proximity to the theoretical prediction derived from geometric optics principles, which is calculated as $d/(2tan\theta)$ = 93.6 mm. Figure 8(c) shows the phase distribution of the extracted wave, which aligns perfectly with the desired phase distribution $\phi(y) = -\alpha\,|y|$. To further investigate the characteristics of the generated Bessel beam, we conducted an analysis of the intensity distributions along the vertical lines indicated in Figs. 8(a) and 8(b). The intensity distributions corresponding to these cross-sections are presented in Figs. 8(d) and 8(e). The intensity distribution of $|E_z|^2$ in Fig. 8(d) closely resembles the zero-order Bessel function $|J_0(\alpha y)|^2$, with a full width at half maximum (FWHM) of 31.4 mm, which is comparable to its theoretical prediction, given by $2.25/\alpha$ = 31.7 mm. Moreover, the intensity distribution of $|H_x|^2$ in Fig. 8(e) matches the profile of the first-order Bessel function $|J_1(\alpha y)|^2$, resembling the characteristics of a three-dimensional Bessel beam with linear polarization. At f = 5.2 GHz, the Bessel beam generating system achieves a transmission efficiency of 95.1%, demonstrating its high performance and suitability for practical applications.

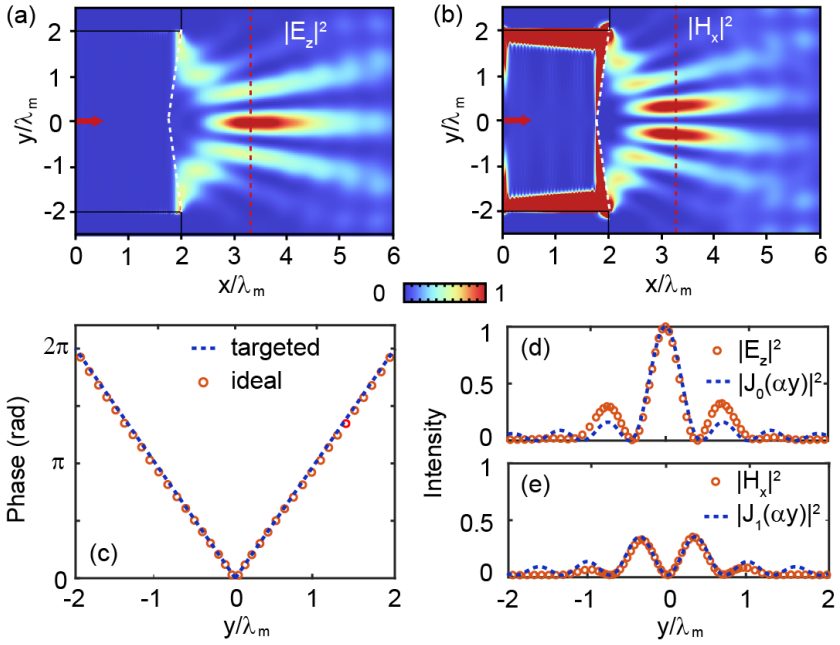

Fig. 8. (a, b) Simulated intensity profiles $|E_z|^2$ and $|H_x|^2$ for generated Bessel beam. (c) The phase distribution of the extracted wave. (d, e) The vertical cut of $|E_z|^2$ and $|H_x|^2$ in (a, b), and the comparison with corresponding Bessel functions $J_0(\alpha y)$ and $J_1(\alpha y)$.

Additionally, LSMPs offer a solution for the issue of transmission efficiency in power splitters. In traditional Y-branch splitters, the power splitting ratio can be tuned by altering the junction region [33,34]. Likewise, LSMP-based splitters facilitate the adjustment of the power splitting ratio. However, LSMP splitters provide additional flexibility in tuning this ratio, including the ability to vary the thickness of the distinct output channels, as illustrated in Fig. 9. In this splitter configuration, both the input and output channels are comprised of LSMP waveguides. The thickness of the input channel is denoted as d, while the thicknesses of the two output channels are represented by d_x and $d - d_x$, respectively. Using the FEM, we simulated wave

Optics EXPRESS

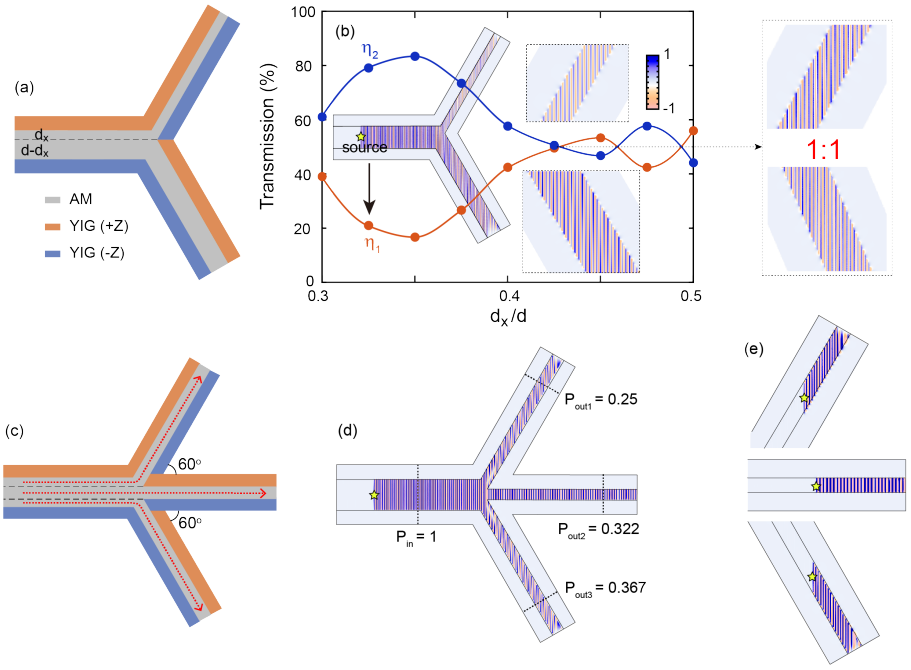

Fig. 9. (a) Schematic of a two-channel Y-branch splitter using LSMP waveguide. (b) The simulated transmission coefficients at the two output ports. The insets are the simulated E-field amplitude for $d_x/d = 0.325$. (c) Schematic of a three-channel Y-branch splitter employing a LSMP waveguide. The splitting ratio can be tuned by adjusting the thickness of the output channels and the angles between adjacent output channels. (d) Simulated E-field amplitude distribution when all individual channels have equal thickness. (e) Simulated E-field amplitude distributions when the excitation source is placed at each output channel.

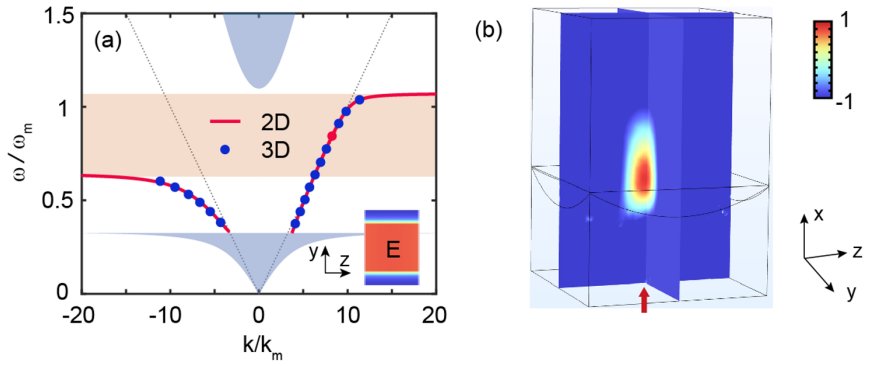

Fig. 10. (a) Dispersion relations for the 2D (solid line) and 3D (solid circles) idea systems. The inset is the modal E-field at 4.3 GHz. (b) Simulated intensity profiles for beam focusing in 3D system.

transmission within the splitter and evaluated the transmission coefficients (η_1, η_2) at the two output ports. These coefficients quantify the proportion of power in the upper output channel (η_1) and the lower output channel (η_2) relative to the power in the input channel. In the simulation, a linear electric current source was utilized to excite LSMPs, positioned centrally within the

Optics EXPRESS

input channel. The parameters used were $d = 2\lambda_m, f = 4.3$ GHz. The simulated transmission coefficients are plotted in Fig. 9(b), revealing that the transmission efficiency varies with the thickness of the output ports. The insets in Fig. 9(b) illustrate the simulated E-field amplitude for $d_x/d = 0.325$ as a representative case. Notably, the splitting ratio (η_1/η_2) can be dynamically tuned by adjusting the thickness of the output channels, offering a straightforward and effective method for optimizing beam distribution. For instance, when $d_x/d = 0.35$, the beam splitting ratio reaches $1:4$; when $d_x/d = 0.425$, the beam splitting ratio becomes $1:1$. The simulated E-field amplitude for the $1:1$ splitting case is illustrated in the right panel of Fig. 9(b). This result underscores the system's potential for precise beam control in practical applications. The design of multi-channel beam splitters presents a significant challenge in beam-splitting applications [35,36]. To demonstrate the versatility of our proposed approach, we developed a multi-channel Y-shaped beam splitter, whose schematic is illustrated in Fig. 9(c). In this configuration, the angles between adjacent output ports are set to 60°, which allows for potential tuning of the splitting ratio by adjusting these angles—a topic that merits further investigation. Figure 9(d) depicts the simulated E-field amplitude distribution within the multi-channel splitting system, where all individual channels have equal thickness. The (normalized) total output power at the three output ports, i.e., $P_{out1} + P_{out2} + P_{out3} = 0.939$, is observed to be slightly lower than the input power $P_{in} = 1$. This discrepancy arises from two primary factors: (1)the inherent energy dissipation due to the lossy nature of YIG, (2)the scattering losses resulting from the abrupt geometric discontinuities at the splitter's junction. Furthermore, because the input and output waveguides operate in a one-way regime, the transmission through each channel is inherently unidirectional. To validate this behavior, we placed excitation sources at each output channel and re-simulated the system. The results, depicted in Fig. 9(e), confirm that when excitation sources are positioned at arbitrary output channels, the excited waves propagate exclusively in the forward direction. This observation substantiates that all output ports exhibit unidirectional transmission.

Finally, the proposed two-dimensional (2D) waveguide can be readily mapped into a three-dimensional (3D) waveguide configuration. In the 2D waveguide, the EM field of SMP extends uniformly along the z-direction, with the E-field oriented in this direction. By truncating the 2D waveguide along the z-axis using a pair of PEC slabs separated by a distance w, the truncated field distributions are preserved within the constructed 3D system. Within the frequency range of interest, if w is smaller than a certain threshold value, this 3D waveguide supports only USMP with a field that is uniform in the z-direction. Consequently, its dispersion relation aligns with that of the original 2D waveguide. To confirm this, we numerically solved for the modes in the ideal 3D system using the FEM. In the simulation, we set $d = w = 4\lambda_m$ and the other parameters were kept consistent with those used in Fig. 4(c). The calculated dispersion relation is plotted as solid circles in Fig. 10(a), which aligns well with the dispersion relation for the 2D system. The inset in Fig. 10(a) displays the E-field amplitudes of the mode in the 3D system at 4.3 GHz, confirming the uniformity of the E-field in both the y- and z-directions. This agreement demonstrates that the truncated 3D waveguide retains the desired field characteristics and dispersion properties of the original 2D waveguide, which allows for the extension of the 2D waveguide analysis and design principles into the realm of 3D waveguide structures. To further validate our framework within the 3D system, we conducted wave focusing simulations using the FEM. Figure 10(b) presents the simulated intensity profile $|E_z|^2$, which clearly demonstrates the anticipated focusing of the extracted wave. These results emphasize the practical relevance of the findings derived from the 2D cases, as they can be effectively extended to 3D scenarios.

5. Conclusions

In conclusion, we present a strategy for realizing tunable LSMPs utilizing a stratified waveguide consisting of AM layers and YIG. By meticulously adjusting system parameters, we have successfully attained a significant unidirectional bandwidth while preserving a large critical

Optics EXPRESS

thickness of LSMPs. In particular, utilizing optimized parameters ($p = 0.495$, $\omega_0 = 0.1\omega_m$), the achieved unidirectional bandwidth reached 2.135 GHz, representing a significant enhancement compared to the 0.15 GHz documented in earlier research, with a critical thickness of 282 mm. Further analysis indicated that the LSMPs in this study displayed a uniform E-field distribution (including amplitude and phase) within the metamaterial layer and exhibited resilience to substantial and complex defects. Based on these unique properties, we validated the potential applications of LSMPs in beam focusing and Bessel beam generation. Significantly, the extensive area coverage of LSMPs provides enhanced flexibility in modulating energy transmission capabilities and attributes. As a result, we developed a tunable Y-shaped beam splitter, which allows for adjustable splitting ratios through the manipulation of the output channel thicknesses. The LSMPs framework presented in this study is relevant to both electrical and optical systems.

Funding. National Natural Science Foundation of China (12404143, 62101496); Start-up Funding of China West Normal University (493117); Luzhou Science and Technology Bureau (2023JYJ046).

Disclosures. The authors declare no conflicts of interest.

Data availability. The data underlying the results presented in this paper are not publicly available at this time, but may be obtained from the authors upon reasonable request.

Supplemental document. See Supplement 1 for supporting content.

References

1. V. G. Veselago, "The electrodynamics of substances with simultan eously negative values of ε and μ," Sov. Phys. Usp. **10**(4), 509–514 (1968).
2. J. Wood, "The top ten advances in materials science," Mater. Today **11**(1-2), 40–45 (2008).
3. R. F. Service and A. Cho, "Strange new tricks with light," Science **330**(6011), 1622 (2010).
4. J. B. Pendry, "Negative refraction makes a perfect lens," Phys. Rev. Lett. **85**(18), 3966–3969 (2000).
5. X. Q. Huang, Y. Lai, Z. H. Hang, *et al.*, "Dirac cones induced by accidental degeneracy in photonic crystals and zero-refractive-index materials," Nat. Mater. **10**(8), 582–586 (2011).
6. J. Pendry, A. Holden, D. Robbins, *et al.*, "Magnetism from conductors and enhanced nonlinear phenomena," IEEE Trans. Microwave Theory Tech. **47**(11), 2075–2084 (1999).
7. D. R. Smith, J. B. Pendry, and M. C. K. wiltshire, "Metamaterials and negative refractive index," Science **305**(5685), 788–792 (2004).
8. M. Wang, W. Zhou, L. Bi, *et al.*, "Valley-locked waveguide transport in acoustic heterostructures," Nat. Commun. **11**(1), 1–6 (2020).
9. Z. Chen, X. Wang, C. W. Lim, *et al.*, "Robust large-area elastic transverse wave transport in active acoustic metamaterials," J. Phys. **131**(18), 185112 (2022).
10. Y. Chen, X. Wen, Y. Lu, *et al.*, "Broadband large-scale acoustic topological waveguides," Compos. Struct. **352**, 118669 (2025).
11. Z. Wang, Y. D. Chong, J. D. Joannopoulos, *et al.*, "Reflection-free one-way edge modes in a gyromagnetic photonic crystal," Phys. Rev. Lett. **100**(1), 013905 (2008).
12. X. Ao, Z. Lin, and C. T. Chan, "One-way edge mode in a magnetooptical honeycomb photonic crystal," Phys. Rev. B **80**(3), 033105 (2009).
13. Z. Wang, Y. D. Chong, J. D. Joannopoulos, *et al.*, "Observation of unidirectional backscattering-immune topological electromagnetic states," Nature **461**(7265), 772–775 (2009).
14. Z. Yu, G. Veronis, Z. Wang, *et al.*, "One-way electromagnetic waveguide formed at the interface between a plasmonic metal under a static magnetic field and a photonic crystal," Phys. Rev. Lett. **100**(2), 023902 (2008).
15. K. L. Tsakmakidis, L. Shen, S. A. Schulz, *et al.*, "Breaking lorentz reciprocity to overcome the time-bandwidth limit in physics and engineering," Science **356**(6344), 1260–1264 (2017).
16. S. A. H. Gangaraj and F. Monticone, "Do truly unidirectional surface plasmon-polaritons exist?" Optica **6**(9), 1158–1165 (2019).
17. M. Wang, R.-Y. Zhang, L. Zhang, *et al.*, "Topological one-way large-area waveguide states in magnetic photonic crystals," Phys. Rev. Lett. **126**(6), 067401 (2021).
18. T. Qu, N. Wang, M. Wang, *et al.*, "Flexible electromagnetic manipulation by topological one-way large-area waveguide states," Phys. Rev. B **105**(19), 195432 (2022).
19. X. Yu, J. Chen, Z.-Y. Li, *et al.*, "Topological large-area one-way transmission in pseudospin-feld-dependent waveguides using magneto-optical photonic crystals," Photonics Res. **11**(6), 1105–1112 (2023).
20. Z. Lan, M. L. N. Chen, J. W. You, *et al.*, "Large-area quantum-spin-hall waveguide states in a three-layer topological photonic crystal heterostructure," Phys. Rev. A **107**(4), L041501 (2023).
21. L. He, Q. Ren, Y. Zhang, *et al.*, "Manipulation for one-way large-area helical waveguide states in topological heterostructure," Phys. Rev. A **135**, 113320 (2023).

Optics EXPRESS

22. P.-Y. Guo, W. Li, J. Hu, *et al.*, "Dual-band topological large-area waveguide transport in photonic heterostructures," Phys. Rev. B **110**(3), 035115 (2024).
23. Y. Yang, X. Qian, L. Shi, *et al.*, "Observation and control of pseudospin switching in a finite-width topological photonic crystal," Opt. Express **30**(4), 5731–5738 (2022).
24. C. Zhang, Y. Ota, and S. Iwamoto, "Wide-mode-area slow light waveguides in valley photonic crystal heterostructures," Opt. Mater. Express **14**(7), 1756–1766 (2024).
25. L. Liang, X. Zhang, C. Wang, *et al.*, "One-way valley-locked waveguide with a large channel achieved by all-dielectric photonic crystal," Opt. Express **32**(13), 23758–23766 (2024).
26. J. Chen and Z.-Y. Li, "Prediction and observation of robust one-way bulk states in a gyromagnetic photonic crystal," Phys. Rev. Lett. **128**(25), 257401 (2022).
27. S. Li, M. L. N. Chen, Z. Lan, *et al.*, "Coexistence of large-area topological pseudospin and valley states in a tri-band heterostructure system," Opt. Lett. **48**(17), 4693–4696 (2023).
28. Q. Shen, X. Zheng, H. Zhang, *et al.*, "Large-area unidirectional surface magnetoplasmons using uniaxial μ-near-zero material," Opt. Lett. **46**(23), 5978–5981 (2021).
29. Q. Shen, J. Yan, Y. You, *et al.*, "Terahertz large area unidirectional surface magnetoplasmon and its applications," Sci. Rep. **13**(1), 21945 (2023).
30. E. Yablonovitch, "Inhibited spontaneous emission in solid-state physics and electronics," Phys. Rev. Lett. **58**(20), 2059–2062 (1987).
31. S. John, "Strong localization of photons in certain disordered dielectric superlattices," Phys. Rev. Lett. **58**(23), 2486–2489 (1987).
32. S. Li, K. L. Tsakmakidis, T. Jiang, *et al.*, "Unidirectional guided-wave-driven metasurfaces for arbitrary wavefront control," Nat. Commun. **15**(1), 5992 (2024).
33. M. Bayindir, B. Temelkuran, and E. Ozbay, "Photonic-crystal-based beam splitters," Appl. Phys. Lett. **77**(24), 3902–3904 (2000).
34. X. Gao, L. Zhou, X. Y. Yu, *et al.*, "Ultra-wideband surface plasmonic y-splitter," Opt. Express **23**(18), 23270–23277 (2015).
35. J. Haines, V. V. K. Bottrill, P. U. Naik, *et al.*, "Fabrication of 1×n integrated power splitters with arbitrary power ratio for single and multimode photonics," Nanophotonics **13**(3), 339–348 (2024).
36. Y. Franz and M. Guasoni, "Compact 1×n power splitters with arbitrary power ratio for integrated multimode photonics," J. Opt. **23**(9), 095802 (2021).